CrystEngComm

PAPER

View Article Online
View Journal | View Issue

Cite this: *CrystEngComm*, 2014, **16**, 2810

Self-decorated $Cu_{2-x}Se$ nanosheets as anode materials for Li ion batteries and electrochemical hydrogen storage†

Dahong Chen,[a] Gang Chen,*[a] Rencheng Jin[b] and Haiming Xu[a]

Received 13th November 2013,
Accepted 6th January 2014

DOI: 10.1039/c3ce42308e

www.rsc.org/crystengcomm

Hierarchical self-decorated $Cu_{2-x}Se$ nanosheets were synthesized through a facile solvothermal route in a binary solution of ethylene glycol and distilled water in the absence of a template. The X-ray diffraction (XRD), scanning electron microscope (SEM), and high-resolution transmission electron microscopy (HRTEM) analyses identified that the as-prepared $Cu_{2-x}Se$ nanosheets were single-crystalline decorated by $Cu_{2-x}Se$ nanodots. Based on the time-dependence experiment, the reaction and growth process was discussed in detail. Furthermore, the electrochemistry Li and hydrogen storage properties of the hierarchical self-decorated $Cu_{2-x}Se$ nanosheets were measured. This hierarchical self-decorated $Cu_{2-x}Se$ nanosheet showed a good cycle and rate performance, indicating its potential application as an anode material for lithium ion batteries. The good cycle and rate performance may be attributed to the unique hierarchical morphology which can buffer the volume change to some degree during the discharging/charging process.

Introduction

In recent decades, the demand for lithium ion batteries (LIBs) with enhanced capacities is increasing due to their widespread application in electric vehicles (EVs) and energy storage systems for renewable energy sources.[1,2] Transition-metal chalcogenides are promising high-performance materials for next-generation LIBs because of their high theoretical capacity, high energy density and high voltage.[3] Among them, copper-based chalcogenide nanocrystals and related alloys have been widely investigated due to their nontoxicity, low cost, and ability to achieve band-gap energies of 1.0–1.5 eV.[4] In particular, many efforts have been devoted to the synthesis of copper selenide because it is a promising candidate for use in thermoelectric converters,[5,6] gas sensors,[7] catalysts,[8] rechargeable sodium batteries[9] *etc.* Copper selenides exist as a variety of stoichiometric and nonstoichiometric compounds such as CuSe, Cu_3Se_2, Cu_5Se_4, $Cu_{1.8}Se$, Cu_2Se, $CuSe_2$, and $Cu_{2-x}Se$.[7] Among them, $Cu_{2-x}Se$ shows unique structures and properties.

$Cu_{2-x}Se$ has Se atoms in a simple face-centred cubic (*fcc*) structure with the space group *Fm*3*m*, but the superionic Cu ions are kinetically disordered throughout the structure, resulting in a quite high electrical conductivity.[10] Thus, researchers are concentrated on the synthesis of $Cu_{2-x}Se$ with different sizes and shapes through various techniques. For instance, $Cu_{2-x}Se$ nanocrystals were fabricated *via* a convenient hydrothermal process using an ionic liquid precursor.[11] Li *et al.* prepared dendritic nanocrystals of $Cu_{2-x}Se$ *in situ* by using alcohol as the solvent.[12] Nanocrystallites of nonstoichiometric $Cu_{2-x}Se$ were synthesized *via* sonochemical irradiation at room temperature.[13] Therefore, researches on the synthesis of $Cu_{2-x}Se$ with new morphologies are still in great demand. Recently, Cu_2Se, CuSe, and $CuSe_2$ have been reported to be potential materials for Li-ion batteries.[14] However, to best of our knowledge, there is no report on the electrochemical properties of $Cu_{2-x}Se$.

Two dimensional nanoarchitectures are considered to be excellent electrodes in lithium storage for energy-storage devices, in particular lithium-ion batteries, due to their shortened paths for fast lithium ion diffusion and large exposed surface offering more lithium-insertion channels.[1] However, the large volume change of the transition-metal chalcogenides during the lithiation and delithiation process has resulted in a poor cycling performance and rate capability, which hampers its widespread commercialization in high-performance LIBs. Thus, novel 2D structures such as flower-like structures assembled by nanosheets,[15,16] sandwich-like nanosheets,[17,18] and ultrathin nanosheets,[19] have been fabricated to enhance the cycling and rate performances. Herein, we report the preparation of a new kind of hierarchical self-decorated $Cu_{2-x}Se$ nanosheets *via* a one-pot solvothermal process in a mixture of ethylene glycol and distilled water. The hierarchical self-decorated $Cu_{2-x}Se$ nanosheets show an excellent cycling and rate performances

[a] *Department of Chemistry, Harbin Institute of Technology, Harbin, 150001, People's Republic of China. E-mail: gchen@hit.edu.cn; Fax: +86 451 86413753; Tel: +86 451 86413753*
[b] *School of Chemistry & Materials Science, Ludong University, Yantai, 264025, People's Republic of China*

† Electronic supplementary information (ESI) available. See DOI: 10.1039/c3ce42308e

as an anode material for LIBs. This is mainly due to the special morphology which can increase the interfaces between the electrode and electrolyte providing more lithium-insertion active sites. The possible growth mechanism is proposed on the basis of time-dependent experiments. In order to determine the optimal synthesis conditions, some reaction parameters such as the volume ratio of ethylene glycol and distilled water, and the amount of NaOH are systematically investigated. Moreover, the electrochemical hydrogen storage behaviors of the hierarchical self-decorated $Cu_{2-x}Se$ nanosheets are measured.

Experimental section

Synthesis

All reagents were analytically pure and used without further purification. In a typical procedure, 0.09 g of sodium selenite, 0.18 g of copper acetate and 0.2 g of sodium hydroxide were dissolved in a mixture of 10 mL of ethylene glycol (EG) and 20 mL of distilled water. After stirring for 30 min, 2 mL of hydrazine hydrate (80%) was added to the above solution. The color of the solution quickly changed from blue to black. The solution was transferred into a 40 mL Teflon-lined stainless-steal autoclave with *ca.* 80% of the total volume filled after stirring for another 5 min. The autoclave was sealed and placed in the oven at 140 °C for 12 h and then cooled to room temperature naturally. The final precipitates were centrifuged, washed with distilled water and absolute ethanol several times, and then dried at 60 °C for 8 h in a vacuum.

Characterization

The X-ray diffraction (XRD) patterns were obtained by a Rigaku-D/MAX-2550PC diffractometer using Cu-Kα radiation. The scanning electron microscopy (SEM) and transmission electron microscopy (TEM) images of the as-prepared samples were collected by employing an FEI Quanta 200F field emission scanning electron microscope and an FEI Tecnai G2 S-Twin transmission electron microscope, respectively.

Electrochemical Li-ion storage measurements

Electrochemical characterization was carried out by 2025 type coin cells in which lithium metal foil was used as the counter electrode. The working electrodes were prepared by mixing the as-synthesized powder, acetylene black and polyvinylidene fluoride (PVDF) with a weight ratio of 80 : 10 : 10 and dissolved it in an *N*-methylpyrrolidinone (NMP) solvent to form a homogenous slurry. The slurry was spread on copper foil current collectors after 6 h stirring, and then dried in a vacuum oven at 120 °C for 12 h. After that, the coated electrodes were pressed at 6 MPa pressure to avoid ecclasis. The test cells were assembled in an argon-filled glove box. The cells were assembled with the as-prepared working electrode, lithium foil as the counter electrode, and Celgard 2400 film as the separator. 1 M $LiPF_6$ in a mixture of ethylene carbonate and diethyl-carbonate (wt/wt = 1 : 1) was used as the electrolyte. The galvanostatic charge and discharge performance was measured between 0.01 and 3.0 V at current densities of 50, 100, 200 and 500 mA g^{-1}, using a NEWARE BTS-610 (Neware Co., Ltd, China) battery tester. The specific capacities were calculated based on the total weight of the active materials. Cyclic voltammetry (CV) at a scan rate of 0.5 mV s^{-1} and electrochemical impedance spectroscopy (EIS) were performed on a CHI604C (Shanghai Chenhua instrument company, China) electrochemical workstation.

Electrochemical hydrogen storage measurements

The electrochemical hydrogen storage measurements were performed following the reported method with a minor modification.[20,21] The as-obtained powder was directly pressed into a circular sheet of nickel foam under 20 MPa pressure (20 mm in diameter and about 1 mm thick). All of the experiments were carried out in a three-electrode cell in 6 M KOH at room temperature in air, in which the $Cu_{2-x}Se$ powders were used as the working electrode, $Ni(OH)_2$/NiOOH was used as the counter electrode, and Hg/HgO was used as the reference electrode. The electrode was charged for 4 h at a current density and discharged at the same current density after a 60 s rest. The electrochemical hydrogen storage experiments were performed on a Land battery system (CT2001A), and cyclic voltammogram measurements were carried out on a CHI604C electrochemical workstation.

Results and discussion

Characterization of $Cu_{2-x}Se$ nanosheets

The powder X-ray diffraction (XRD) technique was employed to analyze the composition and crystal phase purity of the synthesized products. Fig. 1a shows the XRD pattern of the as-prepared $Cu_{2-x}Se$ particles. All peaks can be indexed to the cubic crystal structure of $Cu_{2-x}Se$ (JCPDS no: 06-0680). No impurity peaks are detected. It is worth noting that the

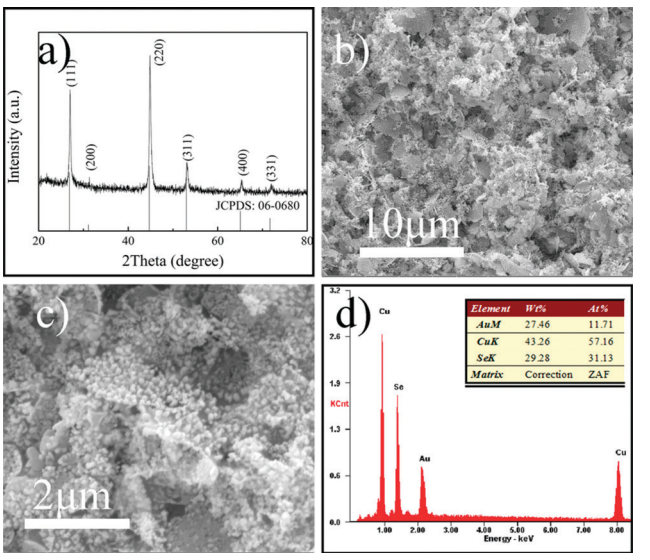

Fig. 1 (a) The XRD pattern, (b) SEM image, (c) high resolution SEM image and (d) EDS spectrum of the as-prepared $Cu_{2-x}Se$ nanosheets.

overall shape of the peaks is asymmetric, which is a characteristic feature of 2D nanosheet structures.[22]

The morphologies of the as-prepared products were examined by SEM observations. The SEM images of particles obtained at 140 °C for 12 h are displayed in Fig. 1b, c. Fig. 1b shows that the as-prepared $Cu_{2-x}Se$ samples are composed of a large quantity of nanosheets with anchored nanoparticles. In the enlarged SEM image (Fig. 1c), the diameter and thickness of the $Cu_{2-x}Se$ nanosheets are ~3 μm and ~50 nm, respectively. Uniform nanoparticles with the size of ~50 nm distribute on the nanosheets. The chemical composition of the $Cu_{2-x}Se$ nanosheets is further characterized by energy-dispersive spectroscopy. Both Se and Cu can be detected in the EDS spectrum (Fig. 1d), and the atom ratio of Cu/Se is about 1.84 : 1, which is consistent with the XRD result.

In order to further obtain detailed information about the micro-structure and morphology of the as-synthesized samples, TEM observations were carried out. The TEM image of the as-obtained products displayed in Fig. 2a further demonstrates the $Cu_{2-x}Se$ nanosheets with a thickness of ~30 nm. Fig. 2b presents the HRTEM image taken from the area near a nanoparticle on the $Cu_{2-x}Se$ nanosheet. The obvious fringes with the interplanar spacings of 0.20 nm correspond to the (220) planes of $Cu_{2-x}Se$, indicating the same phase composition of $Cu_{2-x}Se$ nanosheets and nanocrystals. Therefore, the as-synthesized $Cu_{2-x}Se$ nanosheets are called hierarchical self-decorated $Cu_{2-x}Se$ nanosheets. The HRTEM image of a $Cu_{2-x}Se$ nanosheet exhibits clear lattice fringes with a separation of 0.332 nm and a highly crystalline structure (Fig. 2c). This value corresponds to the (111) lattice plane of $Cu_{2-x}Se$. The corresponding selected-area electron diffraction (SAED) pattern, as shown in the image of Fig. 2d, indicates that the nanosheets are monocrystalline, and the diffraction spots can be indexed to the (111), (220) and (311) planes of cubic $Cu_{2-x}Se$, respectively. Thus, the exposed facet can be indexed to the $\{1\bar{1}0\}$ planes.

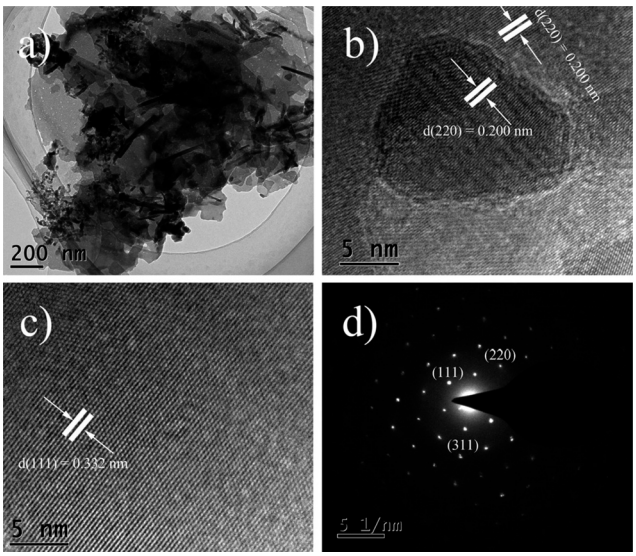

Fig. 2 (a) A TEM image of the as-prepared $Cu_{2-x}Se$ nanosheets, (b) a high resolution TEM (HRTEM) image taken near a decorated nanoparticle, (c) a HRTEM image of a $Cu_{2-x}Se$ nanosheet, (d) the corresponding SAED spectrum of the $Cu_{2-x}Se$ nanosheet.

Growth mechanism

In order to study the growth mechanism of the $Cu_{2-x}Se$ nanosheets, time-dependent experiments were carried out for 30 min, 1 h, 2 h, 3 h and 6 h at 140 °C with the other reaction conditions unchanged. When the reaction time was 30 min, irregular nanocubes were obtained as displayed in Fig. 3a. The corresponding EDS spectrum (Fig. 3b) showed that the signal for the Cu element was much higher than that of the Se element, indicating the lower formation of $Cu_{2-x}Se$. It is worth noting that an obvious O peak can be detected.

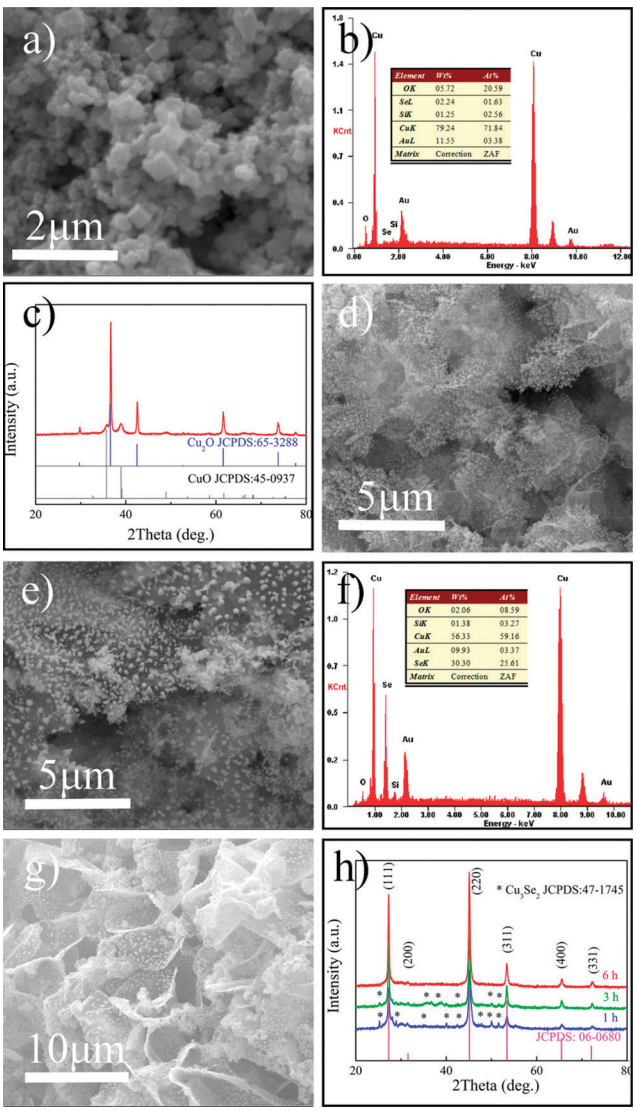

Fig. 3 SEM image of samples prepared for (a) 30 min, (d) 1 h, (e) 3 h, and (g) 6 h, the XRD pattern of particles obtained at 30 min (c), EDS spectrum of samples obtained for (b) 30 min, and (f) 3 h, (h) XRD patterns of products synthesized under different reaction times.

The corresponding XRD pattern of particles obtained at 30 min is shown in Fig. 3c. The XRD peaks revealed that the intermediate products are composed of Cu_2O and CuO. Prolonging the reaction time to 1 h, some nanoplates with nanoparticles were observed (Fig. 3d). Meanwhile, the XRD pattern of products prepared for 1 h (Fig. 3h) revealed the formation of $Cu_{2-x}Se$, and the weak impurity peaks can be indexed to Cu_3Se_2. When the reaction time was further prolonged to 3 h, the nanosheets grew larger (Fig. 3e) and the atom ratio of Cu/Se decreased to nearly 2 : 1 (Fig. 3f), which was close to the final atom ratio of the final products obtained for 12 h (the inset of Fig. 1d). The XRD result displayed that the peak intensity of Cu_3Se_2 became weaker, implying the transformation of Cu_3Se_2 to $Cu_{2-x}Se$ in the samples obtained after 3 h. When the reaction time was increased to 6 h, the $Cu_{2-x}Se$ nanosheets were larger and thicker (Fig. 3g). According to the XRD result (Fig. 3h), all of the peaks can be indexed to $Cu_{2-x}Se$, which demonstrates the purity of the $Cu_{2-x}Se$ nanosheets acquired after 6 h.

Based on the XRD, SEM and EDS results of the time-dependent experiments, the possible formation processes of the hierarchical self-decorated $Cu_{2-x}Se$ nanosheets are schematically illustrated in Scheme 1. According to the XRD data and other reports,[6,11] the possible reaction steps are suggested as follows:

$$Cu^{2+} + 2OH^- \rightarrow CuO + H_2O \quad (1)$$

$$4CuO + N_2H_4 \rightarrow 2Cu_2O + N_2 + 2H_2O \quad (2)$$

$$SeO_3^{2-} + N_2H_4 \rightarrow Se + N_2 + 2OH^- + H_2O \quad (3)$$

$$3Se + 6OH^- \rightarrow 2Se^{2-} + SeO_3^{2-} + 3H_2O \quad (4)$$

$$Cu_2O + CuO + 2Se^{2-} + 2H_2O \rightarrow Cu_3Se_2 + 4OH^- \quad (5)$$

$$(1 - x)Cu_2O + xCuO + Se^{2-} + H_2O \rightarrow Cu_{2-x}Se + 2OH^- \quad (6)$$

$$(2 - x)Cu_3Se_2 \rightarrow 3Cu_{2-x}Se + (1 - 2x)Se \quad (7)$$

In the initial stage of the reaction, the Cu^{2+} ions will react with OH^- and finally form CuO under solvothermal conditions (reaction 1). Meanwhile, CuO will be reduced by N_2H_4 to form Cu_2O (reaction 2). Therefore, nanoparticles composed of CuO and Cu_2O are acquired. With prolonging the reaction time, SeO_3^{2-} will be reduced to Se by N_2H_4 and quickly transform to Se^{2-} in the presence of NaOH (reaction 3 and 4), which is widely reported in the synthesis of selenides.[23] Then, Se^{2-} will react with Cu_2O and CuO, forming Cu_3Se_2 and $Cu_{2-x}Se$ nanosheets (reaction 5 and 6). When the reaction time is prolonged, Cu_3Se_2 will finally transform to $Cu_{2-x}Se$ (reaction 7). On the basis of the evolution of the morphologies observed by the SEM results, the possible growth mechanism of the hierarchical self-decorated $Cu_{2-x}Se$ nanosheets can be explained by an aggregation-based process and ripening growth mechanism. Once the copper selenide nanosheets have been obtained, copper oxide nanoparticles will aggregate onto $Cu_{2-x}Se$ nanosheets in order to minimize the surface energy. With prolonging the reaction time, the decorated copper oxide will further transform into $Cu_{2-x}Se$ nanocrystals. When the reaction time is 6 h, pure hierarchical self-decorated $Cu_{2-x}Se$ nanosheets were generally achieved. In addition, with increasing the reaction time, some small $Cu_{2-x}Se$ nanocrystals cracked and then nucleated onto the $Cu_{2-x}Se$ nanosheets forming final hierarchical self-decorated $Cu_{2-x}Se$ nanosheets through the process known as Ostwald ripening.

Some questions may emerge: why does $Cu_{2-x}Se$ form the sheet morphology? Plate-like $Cu_{2-x}Se$ and its architectures have been synthesized *via* different methods.[6,8] In principle, crystal growth and morphology are attributed to both the intrinsic crystal structure and the extrinsic factors.[24,25] From the structural viewpoint, the shape of a single-crystalline nanostructure is usually a reflection of the symmetry of a basic crystal lattice. The crystal structure of $Cu_{2-x}Se$ with space group $F\bar{4}3m$, as presented in Scheme 1a, exhibits that the Se atoms are packed as a face-center cubic (*fcc*) structure.[26] The Cu atoms could be divided into three types. The first kind of Cu atoms were located at the edges of the Se cubic frameworks. The Cu tetrahedron, which was formed by five Cu atoms of the second kind, was alternately located at the 8c and 32f interstitial positions with the Cu atoms of the third kind. Scheme 1b shows the projected plane representation of the crystal structure along the cubic [1$\bar{1}$0] direction. There are two Cu layers between the neighboring Se (111) planes.[10] Bond breaking along the {1$\bar{1}$0} crystal planes between the Cu layers consumes less energy due to the low density and weak bond strength, resulting in the formation of $Cu_{2-x}Se$ nanosheet exposed {1$\bar{1}$0} facets, which is in accordance with the TEM observations.

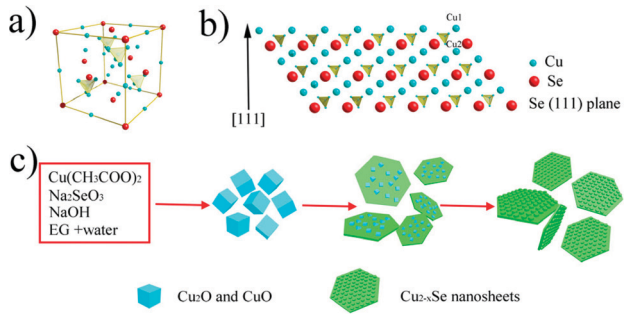

Scheme 1 The schematic diagrams for the growth process of the $Cu_{2-x}Se$ nanosheets.

The influences of the reaction parameters

The ratio of solvent

The volume ratio of the mixed solvent can influence the morphologies of the final products, which have been discussed in our previous works on the preparation of PbTe,[27] Sb_2Se_3,[21] Cu_7Te_4,[25] *etc.*. In this work, the volume ratio of ethylene glycol and water has much effect on the final morphologies of

the products. In the absence of ethylene glycol (V_{EG}: V_{water} = 0 : 30), nanosheets with a diameter of about 10 μm and a thickness of about 100 nm are obtained, and the nanopaticles distribute on the nanosheet uniformly (Fig. 4a). When 5 mL ethylene glycol was added to the reaction system (V_{EG}: V_{water} = 5 : 25), numerous irregular nanosheets and irregular nanocrystals were synthesized, as displayed in Fig. 4b. With 10 mL ethylene glycol in the solution (V_{EG}: V_{water} = 10 : 20), the uniform hierarchical self-decorated $Cu_{2-x}Se$ nanosheets were acquired, as described above (Fig. 1b, c). On further increasing the content of ethylene glycol to 15 mL (V_{EG}: V_{water} = 15 : 15), the products were composed of nanosheets with a diameter up to about 10 μm and irregular nanosheets (Fig. 4c). When the content of ethylene glycol was 20 mL (V_{EG}: V_{water} = 20 : 10), the nanosheets disappeared and only irregular particles can be gained (Fig. 4d). If the solution is a mixture of 25 mL ethylene glycol and 5 mL distilled water (V_{EG}: V_{water} = 25 : 5), few sheets with irregular nanoparticles coexisted (Fig. 4e). Fig. 4f reveals the samples synthesized in the absent of water (V_{EG}: V_{water} = 30 : 0), implying the composition of irregular nanosheets and nanocrystals. In order to demonstrate the phase composition of the samples synthesized in different volume ratios of ethylene glycol/water, an XRD technique was employed. As displayed in Fig. S1,† all of the XRD peaks can be detected to the $Cu_{2-x}Se$ phase, indicating the pure phases of the products obtained in different solvents. Based on the SEM images above, we can conclude that uniform $Cu_{2-x}Se$ nanosheets can only be obtained with the presence of a certain amount of water. The main reason for these results may be due to the different physical and chemical properties of binary solvents, which can influence the solubility, reactivity and diffusion behavior of the reagents and the intermediates. In our system, the properties of the OH^- anions in different solvents should be considered. NaOH can ionize fully in water, and the OH^- anions are highly active. Therefore, with a higher concentrations of ethylene glycol, less OH^- anions exist in the solution, which will decelerate the generation of the $Cu_{2-x}Se$ nanosheets.

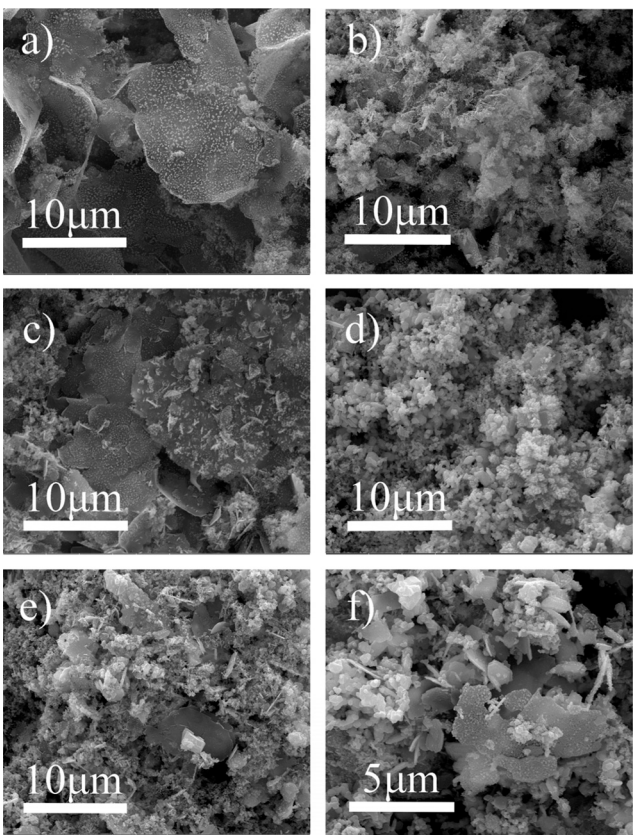

Fig. 4 SEM images of the $Cu_{2-x}Se$ nanosheets synthesized through a solvothermal process in different volume ratios of ethylene glycol/water (*R*), (a) *R* = 0/30, (b) *R* = 5/25, (c) *R* = 15/15, (d) *R* = 20/10, (e) *R* = 25/5, (f) *R* = 30/0.

The amount of NaOH

NaOH has been reported to play an important role in regulating the morphologies of nanocrystals. For instance, PbTe cubic hopper crystals, hierarchical crystals and dendritic structures were adjusted by changing the concentration of NaOH.[28] Hence we also investigate the influence of NaOH *via* regulating the mass of NaOH to 0 g and 0.4 g. Fig. 5a shows the SEM image of $Cu_{2-x}Se$ prepared with the absence of NaOH, indicating that only irregular particles can be obtained without NaOH. When 0.4 g NaOH is added, $Cu_{2-x}Se$ nanosheets with nanoparticles appear in Fig. 5b. However, the size and the distribution of the nanoparticles are uneven, which further implies that the quantity of NaOH should be moderate, too little and too much may change the morphologies of the nanosheets.

Electrochemical properties

The reversible Li storage behavior and cyclic performance of the hierarchical self-decorated $Cu_{2-x}Se$ nanosheet electrode were revealed by galvanostatic cycling measurements. Fig. 6a presents the first three and tenth galvanostatic charging and discharging curves of the $Cu_{2-x}Se$/Li cell cycled between 0.01 V–3.0 V at a current density of 50 mA g^{-1}, indicating the discharging capacities of 397, 287, 228 and 148 mA h g^{-1}, respectively. The large discharge capability may be attributed to the large surface area and the decorated $Cu_{2-x}Se$ nanoparticles, which makes the Li ions deintercalate and intercalate easily because of the very short diffusion distance. Meanwhile, the discharge capacity of the $Cu_{2-x}Se$/Li cells fade fast in the initial several cycles, only about 37% of the initial capacity are

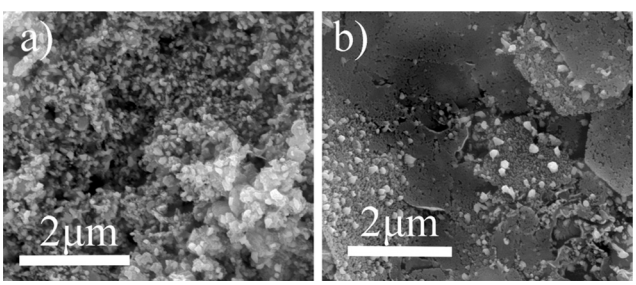

Fig. 5 SEM images of $Cu_{2-x}Se$ prepared with different amounts of NaOH (a) 0 g (b) 0.4 g.

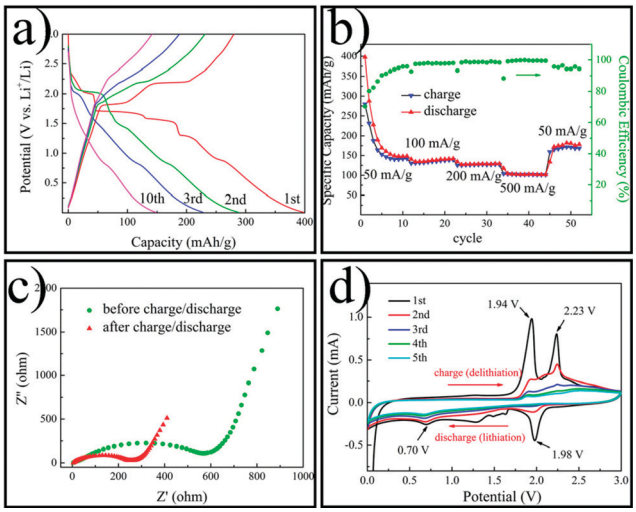

Fig. 6 (a) The first three and tenth-cycle discharging–charging curves for the $Cu_{2-x}Se$ nanosheets at a current density of 50 mA g^{-1} between 0.01 and 3.0 V, (b) the charge–discharge capacity and Coulombic efficiency of the $Cu_{2-x}Se$ nanosheets at different current densities, (c) the electrochemical impedance spectroscopy (EIS) of the $Cu_{2-x}Se$ nanosheet electrodes before and after cycling measurements, (d) the cyclic voltammogram of the $Cu_{2-x}Se$ nanosheets for the first five cycles.

reserved after 10 cycles, indicating a large irreversible capacity loss. The open circuit voltage (OCV) of the cell is near to 3.0 V. In the first discharging profile, two obvious plateaus around 2.0 V and 1.5 V can be observed. The two plateaus (around 2.0 V and 1.5 V) in the discharging curve have been reported in the $CuSe_x$/Li cell,[14] Cu_xS/Cu electrode,[29] hierarchical CuS electrode,[30] *etc.*, which are attributed to the Li-ion insertion into $Cu_{2-x}Se$. The electrochemical reactions can be written as the following:[29–31]

$$2Cu_{2-x}Se + 2xLi \rightarrow (2 - x)Cu_2Se + xLi_2Se \quad (8)$$

$$2Li + Cu_2Se \rightarrow 2Cu + Li_2Se \quad (9)$$

The two plateaus correspond to reactions 8 and 9, respectively. Moreover, when the cycle number is increased to ten, no obvious plateau can be found. Fig. 6b demonstrates the rate capability of the $Cu_{2-x}Se$ nanosheet electrodes from current densities of 50 to 500 mA g^{-1}. The discharging capacities of about 138 and 128 mA h g^{-1} can be obtained at current densities of 100 and 200 mA g^{-1}, respectively. Even at a high current density of 500 mA g^{-1}, the discharging capacity of about 100 mA h g^{-1} is still able to remain, indicating the good rate performance. Furthermore, after the high rate measurements, the specific capacities of the $Cu_{2-x}Se$ nanosheet electrode cycled at 50 mA g^{-1} can recover to about 170 mA h g^{-1}, implying the good reversibility. The capacities of the selenides have been reported to show a fast fading to a very low degree due to the significant volume expansion and contraction during the Li ions repeated insertion/extraction of the anode material.[32] In this work, the unique hierarchical morphology may overcome the volume change to some degree during the discharging–charging process, resulting in a good cycle and rate performance. The Coulombic efficiencies sharply increased from 70% to 95% in the first 10 cycles and maintained nearly 100% in successive runs. Fig. S2† shows the cycle life of the hierarchical self-decorated $Cu_{2-x}Se$ nanosheets. The discharge capacity remains at 210.3 mA h g^{-1} after the 100th cycle, indicating the good cycling performance. The electrochemical impedance spectroscopy (EIS) of the $Cu_{2-x}Se$ nanosheets is displayed in Fig. 6c. It is usually considered that the charge–transfer resistance (R_{ct}) can be signified by the semicircle in the medium-frequency region.[33] The R_{ct} of the $Cu_{2-x}Se$ nanosheet electrode before the cycle measurement was about 580 Ω, however the R_{ct} of the $Cu_{2-x}Se$ nanosheets was reduced to only 250 Ω after the cycle measurement. Fig. 6d shows the first five cyclic voltammogram (CV) curves of the $Cu_{2-x}Se$ nanosheet electrode at room temperature between 0.01 and 3.0 V at a scan rate of 0.5 mV s^{-1}. It is clear that the CV curve of the first cycle is quite different from those of subsequent cycles, especially for the charge branch. In the first discharge cycle, two well-defined peaks at 1.98 and 0.70 V and several irregular peaks around 1.5 V can be observed, which can usually be ascribed to the two steps of the lithiation reactions of the $Cu_{2-x}Se$ nanosheets (1.98 V and around 1.5 V) and nonaqueous electrolyte decomposition during the discharge process (0.7 V).[30] The CV test results are in accordance with the first discharging measurement. Meanwhile, two distinct peaks appear at 1.94 V and 2.23 V during charge. The significant decrease of the peak intensity in the second cycle indicates the occurrence of some irreversible reactions with the formation of an SEI film. It is worth noting that after the first two cycles, the voltage–current curves almost over-lapped, indicating that a stable SEI film formed on the surfaces and interfaces of the $Cu_{2-x}Se$ nanosheets. During the subsequent charge–discharge cycles, the high Coulombic efficiency and the stable and superior reversibility of the products will be acquired.[34]

Electrochemical hydrogen storage properties

Hierarchitectures Sb_2Se_3 nanostructures and Bi_2Se_3 nanospheres have been reported to have a good electrochemical hydrogen storage capacity at room temperature.[21,35] Therefore, the electrochemical hydrogen storage behavior of the hierarchical self-decorated $Cu_{2-x}Se$ nanosheets is measured at a current density of 50 mA g^{-1} at room temperature, and the charge–discharge curves are shown in Fig. 7a. In the charge curve, two obvious plateaus can be observed, which imply the presence of two different hydrogen adsorption sites, in other words, there are two different electrochemical steps in the charging process. The first plateau is found at about 4 mA h g^{-1} (−0.356 V *versus* Hg/HgO) and another obvious plateau is found at about 75 mA h g^{-1} (−0.841 V). The reason was assumed to be as follows: the hydrogen was first adsorbed into the interstitial sites/pores between the $Cu_{2-x}Se$ nanosheets and then entered into the interlayers of the $Cu_{2-x}Se$ nanosheets at high potential. Similar two-potential-plateau phenomena in the charging curve have been reported in other materials, such as carpenterworm-like

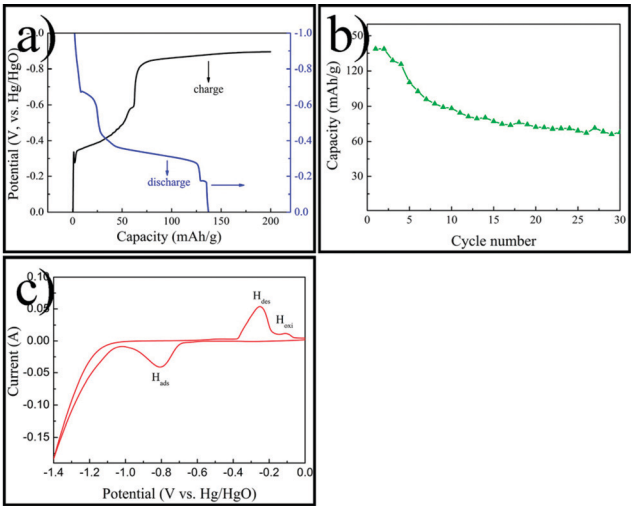

Fig. 7 (a) The charge–discharge curve, (b) cycle life and (c) cyclic voltammogram of the $Cu_{2-x}Se$ nanosheets.

Sb_2Se_3,[21] porous spongelike Ni_2Se,[36] networklike Bi_2S_3[37] *etc.*. The discharge curve displayed in Fig. 7a exists two weak plateaus at *ca.* 8 mA h g^{-1} (−0.678 V), and *ca.* 129 mA h g^{-1} (−0.184 V), respectively, and an obvious plateau at *ca.* 45 mA h g^{-1} (−0.365 V). The electrochemical discharging capacity of 146 mA h g^{-1} can be obtained at 50 mA g^{-1}, implying a potential application in electrochemical hydrogen storage. Moreover, the discharging capacities of 139 mA h g^{-1} and 132 mA h g^{-1} can be reached at 100 mA g^{-1}, and 200 mA g^{-1}, respectively, as shown in Fig. S1.† The electrochemical charging capacities of the MoS_2 nanotube have been reported for 260 mA h g^{-1}, 225mA h g^{-1} and 178 mA h g^{-1} at 50 mA g^{-1}, 100 mA g^{-1} and at 200 mA g^{-1}, respectively.[38] The low charging capacity may be attributed to the lower surface area compared with the MoS_2 nanotube reported before. The cycle life of the $Cu_{2-x}Se$ nanosheet electrode is shown in Fig. 7b. After being cycled 30 times at the charge–discharge current density of 50 mA g^{-1}, the discharging capacity of the $Cu_{2-x}Se$ nanosheets remain over 65 mA h g^{-1}.

In order to further investigate the electrochemical hydrogen adsorption–desorption behavior of the hierarchical self-decorated $Cu_{2-x}Se$ nanosheets, a cyclic voltammogram (CV) was measured. In the CV curve of the $Cu_{2-x}Se$ nanosheets displayed in Fig. 7c, one weak oxidation peak of hydrogen is observed at *ca.* −0.10 V *vs.* Hg/HgO, and one broad desorption peak of hydrogen can be found around −0.25 V, which are essentially consistent with the two plateaus in the discharging curve at −0.28 V and −0.17 V, respectively. Furthermore, the hydrogen desorption peak can also be observed prior to the hydrogen oxidation peak, indicating the possible existence of the strong chemisorption of hydrogen, similar to the observations and discussion on the CVs of ultra-long t-Se submicrotubes.[39] Only one broad reduction peak can be observed at *ca.* −0.81 V *vs.* Hg/HgO during the CV test, which is attributed to the adsorption of hydrogen. Therefore, based on the charge–discharge and CV results, a simple scheme

$$Cu_{2-x}Se + H_2O + e^- \underset{\text{discharge}}{\overset{\text{charge}}{\rightleftharpoons}} (H_{ads} + Cu_{2-x}Se) + OH^-$$

Scheme 2 A possible mechanism for the electrochemical hydrogen storage of the $Cu_{2-x}Se$ nanosheets.

for the adsorption and release of hydrogen is proposed as displayed in Scheme 2.

Conclusion

Hierarchical self-decorated $Cu_{2-x}Se$ nanosheets with a diameter of ~3 μm and a thickness of ~50 nm were synthesized *via* a one-pot solvothermal route in a binary solution without a template. An aggregation-based process and ripening mechanism was put forward to explain the formation of the hierarchical self-decorated $Cu_{2-x}Se$ nanosheets. An appropriate volume ratio of the mixed solvent and a moderate amount of NaOH were considered to be responsible for the formation of the $Cu_{2-x}Se$ nanosheets. The $Cu_{2-x}Se$ nanosheet electrode exhibited a long cycle life and a good rate performance under charge–discharge cycling. Moreover, the hierarchical nanostructures presented high hydrogen storage properties.

Acknowledgements

This work was supported by the National Natural Science Foundation of China (project no. 21071036 and 21271055) and the Province Natural Science Foundation of Heilongjiang Province (ZD201011).

Notes and references

1 J. Liu and X.-W. Liu, *Adv. Mater.*, 2012, **24**, 4097–4111.
2 M. M. Thackeray, C. Wolverton and E. D. Isaacs, *Energy Environ. Sci.*, 2012, **5**, 7854–7863.
3 M.-R. Gao, Y.-F. Xu, J. Jiang and S.-H. Yu, *Chem. Soc. Rev.*, 2013, **42**, 2986–3017.
4 X. Liu, X. Wang, B. Zhou, W.-C. Law, A. N. Cartwright and M. T. Swihart, *Adv. Funct. Mater.*, 2013, **23**, 1256–1264.
5 B. Yu, W. Liu, S. Chen, H. Wang, H. Wang, G. Chen and Z. Ren, *Nano Energy*, 2012, **1**, 472–478.
6 Y. Zhang, C. Hu, C. Zheng, Y. Xi and B. Wan, *J. Phys. Chem. C*, 2010, **114**, 14849–14853.
7 Z. Wang, F. Peng, Y. Wu, L. Yang, F. Zhang and J. Huang, *CrystEngComm*, 2012, **14**, 3528–3533.
8 L. Mi, Z. Li, W. Chen, Q. Ding, Y. Chen, Y. Zhang, S. Guo, H. Jia, W. He and Z. Zheng, *Thin Solid Films*, 2013, **534**, 22–27.
9 Z. Fu, Q. Sun and J. Yue, *Chem. Commun.*, 2013, **49**, 5868–5870.
10 H. Liu, X. Shi, F. Xu, L. Zhang, W. Zhang, L. Chen, Q. Li, C. Uher, T. Day and G. J. Snyder, *Nat. Mater.*, 2012, **11**, 422–425, advance online publication, .
11 X. D. Liu, X. C. Duan, P. Peng and W. J. Zheng, *Nanoscale*, 2011, **3**, 5090–5095.
12 D. P. Li, Z. Zheng, Y. Lei, S. X. Ge, Y. D. Zhang, Y. G. Zhang, K. W. Wong, F. L. Yang and W. M. Lau, *CrystEngComm*, 2010, **12**, 1856–1861.

13 Y. Xie, X. W. Zheng, X. C. Jiang, J. Lu and L. Y. Zhu, *Inorg. Chem.*, 2002, **41**, 387–392.
14 M.-Z. Xue, Y.-N. Zhou, B. Zhang, L. Yu, H. Zhang and Z.-W. Fu, *J. Electrochem. Soc.*, 2006, **153**, A2262–A2268.
15 D. Lei, M. Zhang, B. Qu, J. Ma, Q. Li, L. Chen, B. Lu and T. Wang, *Electrochim. Acta*, 2013, **106**, 386–391.
16 R. Jin, J. Liu, Y. Xu, G. Li, G. Chen and L. Yang, *J. Mater. Chem. A*, 2013, **1**, 10942.
17 X. Wang, X. Cao, L. Bourgeois, H. Guan, S. Chen, Y. Zhong, D.-M. Tang, H. Li, T. Zhai, L. Li, Y. Bando and D. Golberg, *Adv. Funct. Mater.*, 2012, **22**, 2682–2690.
18 J. Liu, J. S. Chen, X. Wei, X. W. Lou and X.-W. Liu, *Adv. Mater.*, 2011, **23**, 998–1002.
19 K. Chang, D. Geng, X. Li, J. Yang, Y. Tang, M. Cai, R. Li and X. Sun, *Adv. Energy Mater.*, 2013, **3**, 839–844.
20 G.-P. Dai, C. Liu, M. Liu, M.-Z. Wang and H.-M. Cheng, *Nano Lett.*, 2002, **2**, 503–506.
21 R. C. Jin, G. Chen, Q. Wang, J. X. Sun and Y. Wang, *J. Mater. Chem.*, 2011, **21**, 6628–6635.
22 J.-W. Seo, Y.-W. Jun, S.-W. Park, H. Nah, T. Moon, B. Park, J.-G. Kim, Y. J. Kim and J. Cheon, *Angew. Chem., Int. Ed.*, 2007, **46**, 8828–8831.
23 S.-Y. Zhang, C.-X. Fang, W. Wei, B.-K. Jin, Y.-P. Tian, Y.-H. Shen, J.-X. Yang and H.-W. Gao, *J. Phys. Chem. C*, 2007, **111**, 4168–4174.
24 W. Shi, J. Yu, H. Wang and H. Zhang, *J. Am. Chem. Soc.*, 2006, **128**, 16490–16491.
25 Q. Wang, G. Chen, D. Chen and R. Jin, *CrystEngComm*, 2012, **14**, 6962–6973.
26 G. Xiao, J. Ning, Z. Liu, Y. Sui, Y. Wang, Q. Dong, W. Tian, B. Liu, G. Zou and B. Zou, *CrystEngComm*, 2012, **14**, 2139–2144.
27 R. Jin, G. Chen, J. Pei, C. Yan, X. Zou, M. Deng and S. Sun, *CrystEngComm*, 2012, **14**, 2327–2332.
28 T. J. Zhu, X. Chen, Y. Q. Cao and X. B. Zhao, *J. Phys. Chem. C*, 2009, **113**, 8085–8091.
29 R. Cai, J. Chen, J. Zhu, C. Xu, W. Zhang, C. Zhang, W. Shi, H. Tan, D. Yang, H. H. Hng, T. M. Lim and Q. Yan, *J. Phys. Chem. C*, 2012, **116**, 12468–12474.
30 Y. Han, Y. Wang, W. Gao, Y. Wang, L. Jiao, H. Yuan and S. Liu, *Powder Technol.*, 2011, **212**, 64–68.
31 Y. Chen, C. Davoisne, J.-M. Tarascon and C. Guery, *J. Mater. Chem.*, 2012, **22**, 5295–5299.
32 H. Xu, G. Chen, R. Jin, J. Pei, Y. Wang and D. Chen, *CrystEngComm*, 2013, **15**, 1618–1625.
33 M. Du, C. Xu, J. Sun and L. Gao, *J. Mater. Chem. A*, 2013, **1**, 7154.
34 C. He, S. Wu, N. Zhao, C. Shi, E. Liu and J. Li, *ACS Nano*, 2013, **7**, 4459–4469.
35 Z. Sun, S. Liufu, X. Chen and L. Chen, *Chem. Commun.*, 2010, **46**, 3101–3103.
36 B. Zhang, X. Ye, W. Dai, W. Hou and Y. Xie, *Chem.–Eur. J.*, 2006, **12**, 2337–2342.
37 B. Zhang, X. C. Ye, W. Y. Hou, Y. Zhao and Y. Xie, *J. Phys. Chem. B*, 2006, **110**, 8978–8985.
38 J. Chen, N. Kuriyama, H. Yuan, H. T. Takeshita and T. Sakai, *J. Am. Chem. Soc.*, 2001, **123**, 11813–11814.
39 B. Zhang, W. Dai, X. C. Ye, W. Y. Hou and Y. Xie, *J. Phys. Chem. B*, 2005, **109**, 22830–22835.